



Designing transparent nanophotonic gratings for ultra-thin solar cells

PHOEBE M. PEARCE,^{1,3,*}  EDUARDO CAMARILLO ABAD,^{1,3}  AND LOUISE C. HIRST^{1,2}

¹Department of Physics, University of Cambridge, CB3 0HE Cambridge, United Kingdom

²Department of Materials Science and Metallurgy, University of Cambridge, CB3 0FS Cambridge, United Kingdom

³These authors contributed equally to this work

*pmp31@cam.ac.uk

Abstract: Integration of a rear surface nanophotonic grating can increase photocurrent in ultra-thin solar cells. Transparent gratings formed of dielectric materials and high bandgap semiconductors can offer efficient diffraction with lower parasitic absorption than more widely studied metal/dielectric equivalents. In these systems, the maximum photocurrent which can be obtained for a grating made of a given combination of materials is shown to follow a simple empirical model based on the optical constants of these materials and independent of grating dimensions. The grating dimensions still require optimization in order to maximize the photocurrent for a given active layer thickness by balancing the effects of diffraction outside the front surface escape cone and the tuning of waveguide modes in long wavelength regions which are poorly absorbed in an ultra-thin film. The optimal grating pitch is shown to be of particular relevance for both effects, changing nonmonotonically as the absorber gets thicker in order to track favourable waveguide mode resonances at wavelengths near the absorber bandgap. These trends together with the empirical model for material selection drastically reduce the design space for highly efficient light trapping with transparent gratings.

Published by Optica Publishing Group under the terms of the [Creative Commons Attribution 4.0 License](https://creativecommons.org/licenses/by/4.0/). Further distribution of this work must maintain attribution to the author(s) and the published article's title, journal citation, and DOI.

1. Introduction

Ultra-thin photovoltaic devices have reduced material usage and the potential for corresponding lower costs than their thicker counterparts. They also enable flexible form factors for systems integration and have intrinsic tolerance to high-radiation environments common in space power applications [1]. Interest in this emerging device concept is currently growing [2,3], with much research being devoted to light management for maximizing absorption of solar illumination, which is an inherent challenge for ultra-thin geometries. One strategy for addressing this challenge is to employ a front surface antireflection coating with a rear surface planar mirror. While this allows (in the ideal case) for a double pass of the absorber regions, outcoupling losses due to light escaping through the front surface of the cell can still be significant with ultra-thin geometries. Light trapping approaches which diffract or scatter light can reduce this outcoupling, offering a further boost to the absorption of sunlight.

Texturing at the nanoscale is a well-known light trapping strategy for thin and ultra-thin solar cells [4]. Periodic nanostructures can be introduced to the device architecture and tailored to control the scattering of incident light and maximize coupling to optical modes which localize the field in the device. Key light trapping mechanisms are (i) the scattering of light outside the escape cone with the incident medium, which prevents power losses to air, and (ii) coupling of light to waveguide modes in the structure, which can highly confine the field in the device's active material. Random texturing can also offer these mechanisms, but lacks control of the scattered

fields and may also scatter power within the escape cone [2], contributing to the outcoupling losses which can be highly detrimental to ultra-thin devices.

Metallic nanostructures have been widely studied as light trapping layers given their strong scattering of light and the high field localization of plasmonic resonances [5,6]. Good performance enhancements have been demonstrated experimentally and theoretically [7,8], but it has also been found that these structures introduce significant parasitic absorption [9]. This additional loss mechanism can be eliminated by employing nanostructures or scattering surfaces made with dielectric materials and/or high bandgap semiconductors that are effectively transparent in the target spectral range. Such a strategy has already been proposed for highly efficient light trapping layers and it is broadly acknowledged that high-index materials would be needed to retain favourable scattering properties [10–14].

Various designs have been proposed for nonmetallic light trapping layers and promising potential has been demonstrated [15]. Front-side nanostructures, for example, can support additional resonances such as whispering gallery modes [16] or Mie resonances [17] that can enhance the coupling of incident light to the adjacent semiconductor material. Besides antireflection properties, these front-side structures can also contribute to light trapping mechanisms [18–21]. Other studies have also analysed the effectiveness of introducing front and rear structures where the device active material itself is nanostructured [15,22–28].

Despite the positive results of these studies, limited attention has been given to the available material space when designing nonmetallic light trapping arrays. Devices with nanostructures of materials like SiO₂, TiO₂, transparent conductive oxides (TCOs), or the absorber material itself have shown photocurrent enhancements compared to equivalent planar devices, but systematic comparisons among different material systems remain scarce. Additionally, the nanostructures must exist within a matrix of another material and the interplay between the nanostructure and matrix properties has not been studied in detail. A better understanding of the potential of nonmetallic light trapping layers and their optimal designs requires addressing this interplay and providing specific criteria to select favourable material combinations, accounting for both real and imaginary parts of their refractive indices. Ultimately, direct comparisons between the performance of metallic and nonmetallic light trapping layers are also needed to establish the conditions under which these strategies can offer the most favourable absorption enhancement.

In this work we study and compare the light trapping potential of nanostructured arrays of a large number of real dielectric and semiconductor materials. We focus on GaAs solar cells and work with nonmetallic rear light trapping layers separate from the absorber material. This approach isolates light trapping mechanisms from antireflection properties, and is applicable to a larger number of device architectures than directly texturing the active layer, which is poorly compatible with ultra-thin absorbers. We begin by optimizing the performance of nonmetallic light trapping layers with different material combinations and for absorber thicknesses in the range of 50 to 300 nm, so that our results are representative of the entire ultra-thin regime. For the optimization process we use rigorous coupled-wave analysis (RCWA) simulations to obtain the photocurrent from the GaAs layer, and a differential evolution (DE) algorithm to find the most favourable grating parameters and maximize the photocurrent for each material combination. Based on the optimized photocurrents obtained from these simulations, we propose a simple empirical model to estimate the light trapping efficiency of an optimal nonmetallic grating made of a given material combination based solely on the optical constants of these materials. The model shows good agreement with simulated data and does not require knowledge of any grating parameters or available optical modes. Our simulations show that with appropriate materials and optimal design, nonmetallic light trapping layers can boost the short-circuit current of an ultra-thin GaAs cell by up to 90% compared to a planar device with a rear mirror, and can also outperform metallic light trapping layers. Finally, we move on to analysing the trends in optimal grating parameters for different absorber thicknesses. Whereas the optimal periodicity of

nanophotonic gratings is normally assumed to be close to the target wavelength for light trapping, we show that this parameter actually varies in accordance with the dispersion of the waveguide modes in the device stack, maximizing mode coupling near the bandgap where the absorption coefficient is low and light trapping mechanisms are essential.

2. Methods

2.1. Device architecture

The device architecture studied in this work is shown in Fig. 1 and is based on the device structure realized in [8]. $\text{In}_{0.49}\text{Ga}_{0.51}\text{P}$ and $\text{In}_{0.47}\text{Al}_{0.53}\text{P}$ passivation layers are used on top and below the GaAs active layer, respectively. A rear grating is located below the $\text{In}_{0.47}\text{Al}_{0.53}\text{P}$ and on top of a back Ag mirror. A single-layer SiO_2 antireflection coating (ARC) is also included at the front of the structure. The grating has a square unit cell which contains a simple square feature, also shown in Fig. 1.

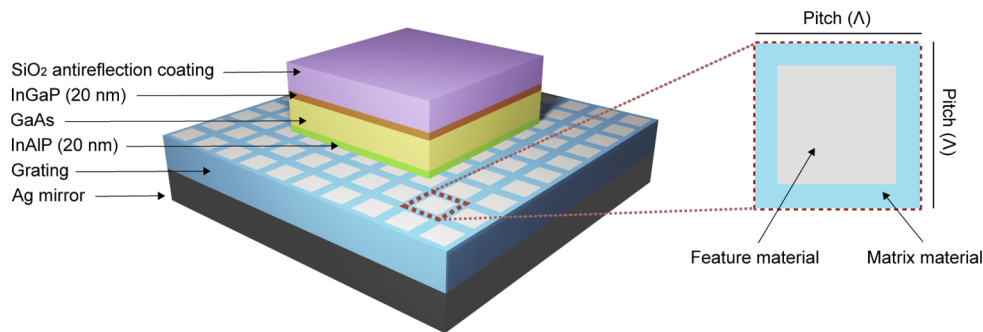


Fig. 1. Device architecture simulated in this work. Light is normally incident from air in the RCWA simulations.

Throughout this work, the thicknesses of the passivation layers are fixed at 20 nm. Different GaAs absorber thicknesses in the ultra-thin regime are studied, as well as different material selections for the square feature and the surrounding matrix in the grating. Table 1 lists the semiconductor and dielectric materials used in the gratings (indicated as such) and for the device layers and Ag back mirror, with the data source for the optical constant values. Figure 2 shows the real (n) and imaginary (κ) parts of the refractive index of each material used in the gratings, in addition to the refractive index for GaAs used for the active layer in the simulated cell structure.

2.2. Optimization procedure

The optimizations presented in the paper are divided into two stages, first optimizing at three discrete GaAs absorber thicknesses (80, 150 and 300 nm) for a large number of material combinations (42 in total). These results were used to fit the empirical model discussed in Section 3. For the second stage of optimizations, a subset of material combinations was chosen and optimized at GaAs thicknesses spanning the range 50-300 nm in 10 nm intervals, to study the behaviour of the optimal current and grating dimensions with GaAs thickness in greater detail.

For a given selection of GaAs thickness and grating materials, four parameters were considered to maximize the absorption of light in the active layer: the pitch, grating and ARC thickness and the size of the square nanostructure in the unit cell of the grating. As a metric for this last parameter, the fill factor is defined as the ratio of the area of the square feature to the area of the unit cell. The figure of merit for the optimization is the short circuit current of the cell assuming

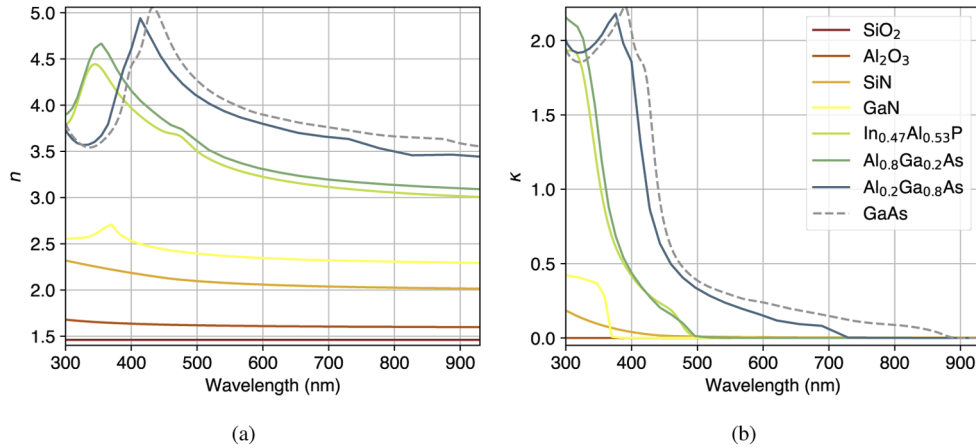


Fig. 2. (a) Real (n) and (b) imaginary (κ) parts of the complex refractive index of the materials used in the diffraction grating simulations, and of the GaAs absorber. Redder colours indicate a more dielectric material (generally lower n and lower κ (higher bandgap) over the wavelength region of interest). The source of the data is given in Table 1.

Table 1. Source of the optical constant data used in the RCWA simulations and waveguide mode analysis. SE refers to spectroscopic ellipsometry and subsequent model fitting as described in [8].

Material	Role	Source	Notes
SiO ₂	Grating/ARC	$n = 1.46, \kappa = 0$	Dispersionless approx.
SiN	Grating	SE (own sample) [8]	Cody-Lorentz model
Al ₂ O ₃	Grating	SE (own sample) [8]	Cody-Lorentz model
Al _{0.8} Ga _{0.2} As	Grating	Ioffe database [29]	Digitized data
Al _{0.2} Ga _{0.8} As	Grating	Ioffe database [29]	Digitized data
GaN	Grating	Yu et al. [30]	Digitized data
In _{0.47} Al _{0.53} P	Grating/Hole barrier	SE (own sample) [8]	Herzinger-Johs model [31]
Ag	Back mirror	Jiang et al. [32]	Drude-Lorentz-Gaussian fit
GaAs	Active layer	SE (own sample) [8]	Herzinger-Johs model
In _{0.49} Ga _{0.51} P	Electron barrier	SE (own sample) [8]	Herzinger-Johs model

100% internal quantum efficiency, calculated according to the following expression:

$$J_{ph} = q \int \Phi(\lambda) A_{\text{GaAs}}(\lambda) d\lambda \quad (1)$$

where $\Phi(\lambda)$ is the photon flux in the AM1.5G solar spectrum as a function of wavelength λ , q is the elementary charge, and $A_{\text{GaAs}}(\lambda)$ is the fraction of incident photons absorbed in the GaAs at each wavelength. The integration is performed between 300 and 930 nm, limited at the short end by the lack of photons in the terrestrial solar spectrum at wavelengths below 300 nm, and by the bandgap of GaAs at the high end. The wavelength-dependent absorption $A_{\text{GaAs}}(\lambda)$ is calculated through RCWA simulations. RayFlare [33] was used to define the structures; the RCWA implementation used by RayFlare is a modified version of S^4 [34]. Further details of the RCWA simulations, and this choice of figure of merit, are given in Supplement 1.

Differential evolution (DE), a type of evolutionary algorithm, was used to search for optimal solutions. In DE, a population of vectors corresponding to the input parameters of the model to be optimized is generated, the fitness of each population is calculated, and then the population

is ‘mutated’ in such a way that the traits of the more successful members of the population are more likely to survive. This is repeated a number of times, generating new populations with improving fitness with each iteration. Further details of the DE method, including the upper and lower bounds for each parameter, are given in [Supplement 1](#).

2.3. Waveguide mode analysis

The waveguide modes supported by the solar cells of interest were calculated with a transfer matrix method (TMM) for the waveguide analysis of multilayered optical stacks [35], using the optical constants included in Table 1. Since the TMM only considers uniform planar layers, the grating was given an effective index calculated based on the the complex refractive indices of the feature and matrix materials, weighted by their volume ratio within the unit cell. The TMM provides dispersion equations for TE and TM polarized light, whose roots correspond to the complex propagation constants of the waveguide modes supported by the stack for the corresponding polarization of light. A Newton-Raphson method was used to solve the roots of the dispersion equations in the complex plane.

3. Optimization of nonmetallic gratings with multiple material combinations

To explore the effectiveness of different material combinations for the grating, the GaAs thickness was initially fixed at 80 nm while for each material combination the grating dimensions (pitch, thickness and fill factor) and ARC thickness were optimized to give maximum J_{ph} . The aim of this is twofold: to identify combinations of materials which will make the best gratings, and to investigate the relationship between the optical constants of the two grating materials and the performance of the optimized grating. Establishing an empirical relationship between the optical constants of the materials used in the grating and the maximum possible performance of such a grating provides a simple method to identify favourable material combinations. It allows the relative magnitude of the maximum achievable current (compared to other material combinations) to be predicted without having to perform computationally intensive simulations.

It is expected that a high contrast between the real part of the refractive indices of the materials will lead to a good grating [10], while high κ values will cause parasitic absorption of photons in the grating layer [9] and thus lead to a lower J_{ph} . To quantify these effects, the basis of the model introduced here is the mean of the real and imaginary parts of the complex refractive index $n(\lambda) + i\kappa(\lambda)$ of the two grating materials between 400 and 900 nm. These are the wavelengths at which light trapping in GaAs is most beneficial; below 400 nm, most incident light is absorbed even in a very thin layer of GaAs due to the high values of α ($= \frac{4\pi\kappa}{\lambda}$). It was observed in the simulation results that the optimized current remained relatively constant if the materials for the feature and matrix were exchanged, as shown in Fig. 3(a), although generally the gratings with positive $\bar{n}_{\text{feature}} - \bar{n}_{\text{matrix}}$ had slightly higher optimized J_{ph} . These correspond to gratings with the material with the lower mean n value (i.e. more dielectric) being the matrix surrounding features with a higher mean n . However, the difference under interchange of the grating materials is < 10% in each case and the direction of the change is not consistent across all material combinations, so in order to keep the model as simple as possible it is constructed to be symmetrical under exchange of the two materials; i.e. if the feature and matrix materials are switched, the predicted optimized current will be the same. Thus, the dependent variables were chosen to be:

$$\Delta n = |\bar{n}_{\text{feature}} - \bar{n}_{\text{matrix}}| \quad (2)$$

$$\Sigma \kappa = \bar{\kappa}_{\text{feature}} + \bar{\kappa}_{\text{matrix}} \quad (3)$$

where the \bar{x} notation indicates taking the mean of the value between 400 and 900 nm. The Δn variable describes the refractive index contrast (i.e. high values should improve the grating’s performance) while the $\Sigma \kappa$ variable is a measure of the expected parasitic absorption (i.e. high

values should degrade the grating's performance). It was found that a good fit to the data could be obtained using a model of the form:

$$J_{ph} = a \ln \Delta n + b \Delta n \Sigma \kappa + c \quad (4)$$

where a , b and c are the fit parameters. Models using other functional forms of Δn and $\Sigma \kappa$ were also tested, but were found to have poorer fit, as discussed in [Supplement 1](#). Figure 3(b) shows the optimized values of J_{ph} , obtained through the DE algorithm in combination with RCWA simulations, compared to the modelled J_{ph} values predicted by the model of the form in Eq. (4). While there is some spread around the dashed line (indicating a perfect fit of the data to the model), the simple model is effective at predicting the optimized J_{ph} . This is remarkable since the optimized J_{ph} values are generated through hundreds of RCWA simulations, while the modelled J_{ph} values are trivial to calculate based on only the refractive indices of the grating materials. Of course, the simple empirical model only predicts what the maximum performance of the grating could be, not the grating design which gives this optimal current; however, by eliminating a large number of material combinations, it can narrow down the parameter space significantly. As for the optimal grating design, it will be shown in Section 5 that this can be explained by considering the dispersion of waveguide modes, allowing predictions of favourable parameters. Note that material combinations which give an optimized result for J_{ph} which is lower than the J_{ph} for an equivalent device with only a planar Ag back mirror (5 out of 42 material combinations) were excluded from the fits in Fig. 3(b): in this case, the optimal case is a grating thickness of zero, so neither of the grating materials is actually present and the model in Eq. (4) no longer applies. This issue, and ways it can be avoided, are discussed further in [Supplement 1](#).

While Eq. (4) is an empirical model, the origin of each term and the signs of the coefficients a , b and c can be understood on physical grounds. For the first term, it is expected that a larger contrast between the refractive indices of the material leads to a more efficient grating, and thus a is a positive constant. The logarithmic dependence is consistent with the fact that improving the grating beyond a certain point has diminishing returns, as there is a finite number of solar photons which can be turned into current in the GaAs. The second term is a cross term multiplying Δn and $\Sigma \kappa$; higher κ in either of the materials present in the grating is expected to lead to more parasitic absorption, and thus b is negative. Including the cross term gives a better fit to the data than simply a linear term in κ ; a proposed physical mechanism for this is that if the Δn of the grating is higher, diffraction into the allowed orders is more efficient and thus more photons are expected to propagate in the grating, which can be absorbed parasitically if $\Sigma \kappa$ is non-zero. Finally, the constant c is positive and reflects that even with no grating present, some amount of current will be generated in the 80 nm of GaAs due to the first pass and reflection at the rear Ag mirror.

To investigate whether such an empirical model is valid for other absorber thicknesses, the same optimization procedure was carried out for each grating material combination at GaAs absorber thicknesses of 150 nm and 300 nm; the results and a fit to Eq. (4) are shown in Fig. 3(c) and (d) respectively. Table 2 shows the values of a , b and c fitted to the data at the three different GaAs thicknesses. The GaAs thickness clearly changes fit parameters obtained, but the trend observed is in accordance with the physical interpretation as discussed; as the GaAs gets thicker, the impact of the grating on the current is reduced and the magnitudes of a and b decrease, while the magnitude of the constant offset c increases. The full optimization results at all three thicknesses are shown in [Supplement 1](#). Note that this model is only valid for non-metallic gratings (i.e. $\epsilon_1 > 0$ over the wavelength range of interest); however, it is possible to construct a similar model for the optimized performance of metal gratings [9].

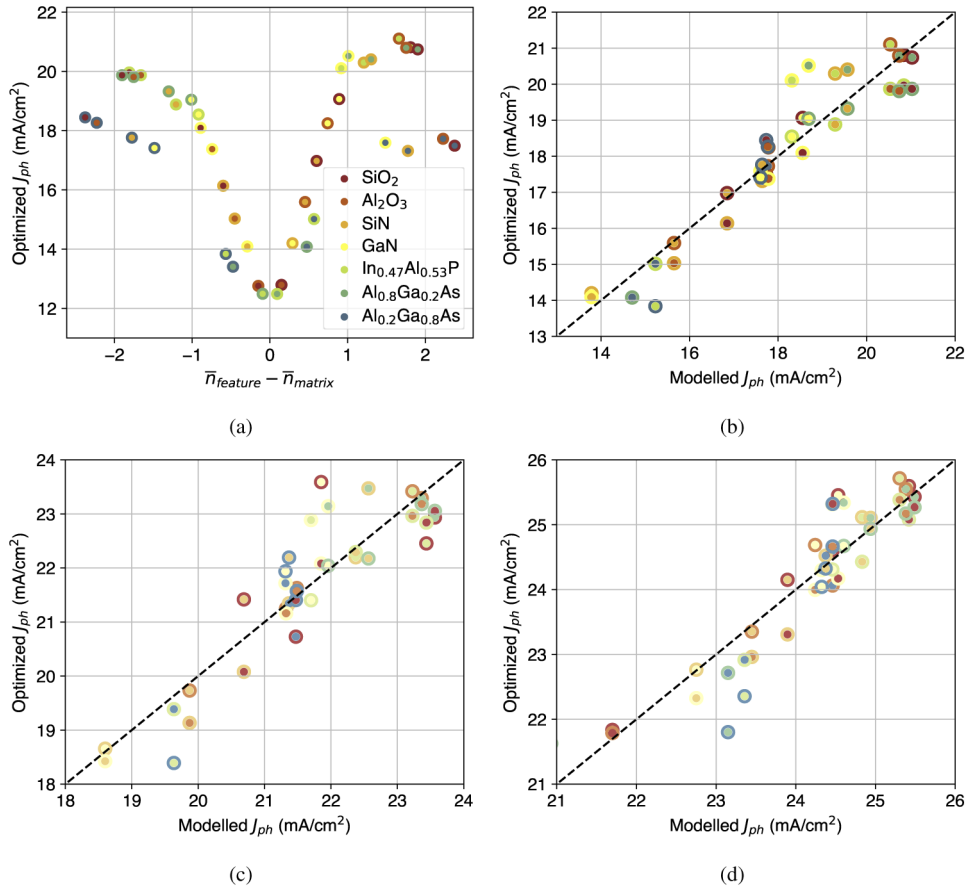


Fig. 3. (a) Optimized J_{ph} values for the different material combinations, obtained through the DE optimization process, vs. the difference in the mean refractive index values over the wavelength range 400-900 nm (\bar{n}) of the feature and the matrix material (if the feature and matrix materials are switched, \bar{n} changes sign). (b)-(d) show the photogenerated current as obtained by optimizing the solar cell structures (optimized J_{ph}) and from the empirical model (modelled J_{ph}) shown for (b) 80 nm of GaAs, (c) 150 nm of GaAs and (d) 300 nm of GaAs. The different colours indicate different materials; the outer part of the circle shows the matrix material while the inner part is the grating material. As in Fig. 2, redder colours generally indicate a higher bandgap and lower values of n , i.e. the material is ‘more dielectric’.

Table 2. Parameters fitted to the data using Eq. (4) at three different thicknesses of the absorbing GaAs layer, with the normalized root mean square deviation (NRMSD).

GaAs thickness (nm)	Parameter			NRMSD
	a	b	c	
80	4.24	-9.58	19.05	0.096
150	2.89	-6.19	22.18	0.082
300	1.58	-3.122	24.715	0.083

4. Nonmetallic grating optimization across different length-scales

The results of the previous section indicate that the performance of a material combination in a grating is relatively consistent across the three GaAs thicknesses considered (80 nm, 150 nm and 300 nm). In this section, a subset of the material combinations is considered across GaAs length scales in more detail. As before, the grating dimensions were optimized to maximize J_{ph} at each GaAs thickness, scanning across the range of 50 to 300 nm in 10 nm steps. It was observed in the results presented in the previous section that the ARC thickness did not significantly influence the simulated current, and thus to reduce the parameter space and improve convergence it was fixed at 100 nm. Four sets of material combinations were chosen to cover gratings with good, intermediate, and poor performance.

Figure 4(a) shows how the optimized current for these material combinations varies across the range of GaAs thicknesses, also showing the performance of a device structure with only a planar Ag mirror at the rear for comparison. We see that the all-dielectric (Al_2O_3 and SiN) grating has the worst performance across the full range, while the $\text{SiO}_2/\text{Al}_{0.8}\text{Ga}_{0.2}\text{As}$ and $\text{Al}_2\text{O}_3/\text{In}_{0.47}\text{Al}_{0.53}\text{P}$ gratings made of a dielectric and a high-bandgap semiconductor with high refractive index contrast (Fig. 2) have the best performance (the order of materials is given as matrix material/feature material throughout). The $\text{SiO}_2/\text{Al}_{0.2}\text{Ga}_{0.8}\text{As}$ gratings give intermediate performance; while the refractive index contrast between SiO_2 and $\text{Al}_{0.2}\text{Ga}_{0.8}\text{As}$ is actually higher over the wavelength range of interest than that between SiO_2 and $\text{Al}_{0.8}\text{Ga}_{0.2}\text{As}$ (see Fig. 2(a)), the $\text{Al}_{0.2}\text{Ga}_{0.8}\text{As}$ has non-negligible absorption up to $\lambda \approx 700$ nm which negatively affects its performance. The highest-performing material combinations ($\text{SiO}_2/\text{Al}_{0.8}\text{Ga}_{0.2}\text{As}$ and $\text{Al}_2\text{O}_3/\text{In}_{0.47}\text{Al}_{0.53}\text{P}$) also outperform optimized metallic SiN/Ag gratings at all GaAs thicknesses considered. Focusing specifically on the data for 80 nm GaAs thickness from the previous section, 12 of the 42 material combinations outperform the optimized SiN/Ag or Ag/SiN grating. The material combinations which outperform the metallic grating have a mean value of Δn of 1.56 (s.d. 0.34) and a mean value of $\Sigma\kappa$ of 0.042 (s.d. 0.002), compared to a mean Δn and $\Sigma\kappa$ of 1.13 (0.65) and 0.088 (0.09) respectively for the whole population of material combinations. This shows that well-performing gratings have higher refractive index contrast and lower κ . The minimum value of Δn was 0.093 for the whole population and 0.92 for the gratings outperforming the Ag/SiN case, while the maximum value of $\Sigma\kappa$ was 0.26 in the whole population and 0.048 in the better gratings. Exchanging the materials used for the matrix and grating features gives similar optimized current results, as seen in Fig. 4(b) for gratings made of Al_2O_3 and $\text{In}_{0.47}\text{Al}_{0.53}\text{P}$. Full results and optimized parameters obtained for all the material combinations are shown in Supplement 1.

The J_{ph} generally shows an increase with increasing GaAs thickness, as expected, but there are some local maxima or consecutive points where the optimal J_{ph} remains constant with increasing thickness. Figure 4(a) shows that these features also occur in the case of a structure with a planar Ag mirror at the rear, indicating that at least for the planar case these features are due to more favourable Fabry-Perot interference (i.e. causing a peak in absorption in GaAs at a wavelength in the range 400-900 nm) occurring for some GaAs thicknesses. For the structures with gratings, the local maxima are somewhat shifted from the planar Ag case, as is to be expected due to the inclusion of an additional grating layer with a thickness between 50 and 250 nm. For the SiN/Ag grating, the location of the local maxima (around 100 and 240 nm) is similar to the planar Ag case, indicating that favourable Fabry-Perot interference is the most likely explanation for these features. While the exact ordering of the grating performance changes with thickness, gratings which perform well at 50 nm continue to do so up to 300 nm and vice versa. As the GaAs thickness increases the importance of the grating diminishes; the offset between the best and worst-performing gratings decreases. This is also reflected in the reduction of the coefficients a and b in Table 2. The largest current enhancement relative to the planar Ag structure was observed for the $\text{SiO}_2/\text{Al}_{0.8}\text{Ga}_{0.2}\text{As}$ grating at 50 nm GaAs thickness, increasing the J_{ph} from 9.2

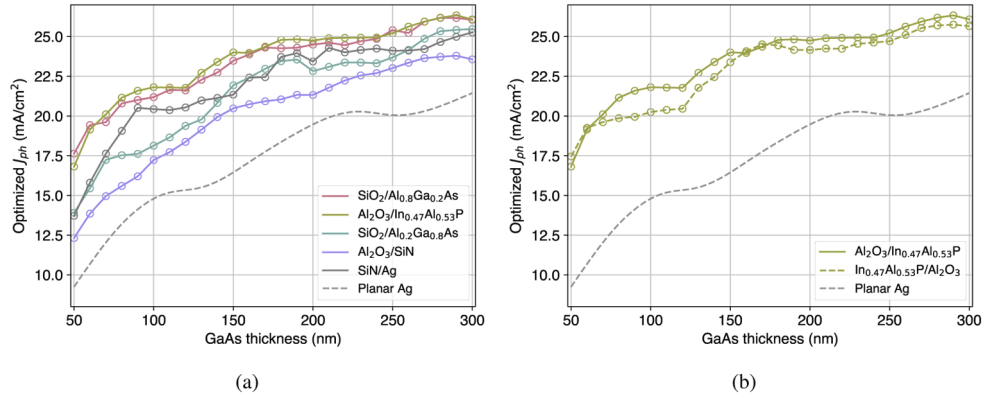


Fig. 4. (a) Optimized J_{ph} as a function of GaAs thickness for several dielectric/high bandgap semiconductor material combinations, an all-dielectric $\text{Al}_2\text{O}_3/\text{SiO}_2$ grating, and a dielectric/metal grating (SiN/Ag). The labelling indicates matrix material/feature material. (b) Shows the data for the $\text{Al}_2\text{O}_3/\text{In}_{0.47}\text{Al}_{0.53}\text{P}$ grating as in (a) in comparison with the results for a grating with the materials reversed ($\text{In}_{0.47}\text{Al}_{0.53}\text{P}$ as the matrix material and Al_2O_3 as the feature material). The dashed line in both plots shows the photogenerated current for a structure with no grating and only a planar Ag mirror at the rear.

mA/cm^2 to $17.6 \text{ mA}/\text{cm}^2$, a 91% increase. At 300 nm GaAs thickness, the increase in current due to the two best gratings is 21.5%.

5. Optimal pitch trends for different absorber thicknesses

It is widely recognized that an optimal light trapping layer must prevent diffraction within the escape cone with the incident medium at poorly absorbed wavelengths close to the absorber bandgap, as these wavelengths require the highest absorption enhancement from light trapping mechanisms. Diffraction within the escape cone occurs whenever the in-plane wavevector (perpendicular to the stacking direction) of diffracted light is shorter than its free-space wavevector ($k_0 = 2\pi/\lambda$), since under such conditions total internal reflection at the interface with air does not take place. For a 2D grating with a square unit cell, the in-plane wavevectors K_{xy} of diffracted light in each available optical state (i.e. diffracted order) are fixed by the periodicity of the lattice according to the following equation (assuming normal light incidence):

$$K_{xy} = \frac{2\pi}{\Lambda} \sqrt{m_1^2 + m_2^2} \quad (5)$$

where Λ is the pitch, and m_1 and m_2 are pairs of integers which describe the optical states. Since different pairs of m_1 and m_2 will yield the same in-plane wavevector in Eq. (5), we group those optical states in sets and label them OS x , with x being the value inside the square root in Eq. (5) (see Fig. 5(a)). Equation (5) shows that for a grating with a square unit cell, all light with a wavelength shorter than the pitch will be poorly trapped within the device since in this case at least one diffracted order (OS1) will lie within the escape cone (i.e. at least OS1 will have $K_{xy} < k_0$). On the other hand, all light with a wavelength larger than the pitch will experience good light trapping since no OS will have $K_{xy} < k_0$, and so all diffracted power will lie outside the escape cone. As a consequence, for the case of a square unit cell the pitch plays a key role by defining an equivalent 'threshold wavelength' for good and poor light trapping.

This observation has led to the assumption that the optimal pitch should be close to a 'target' wavelength for light trapping, so that all wavelengths longer than the threshold (i.e. longer than

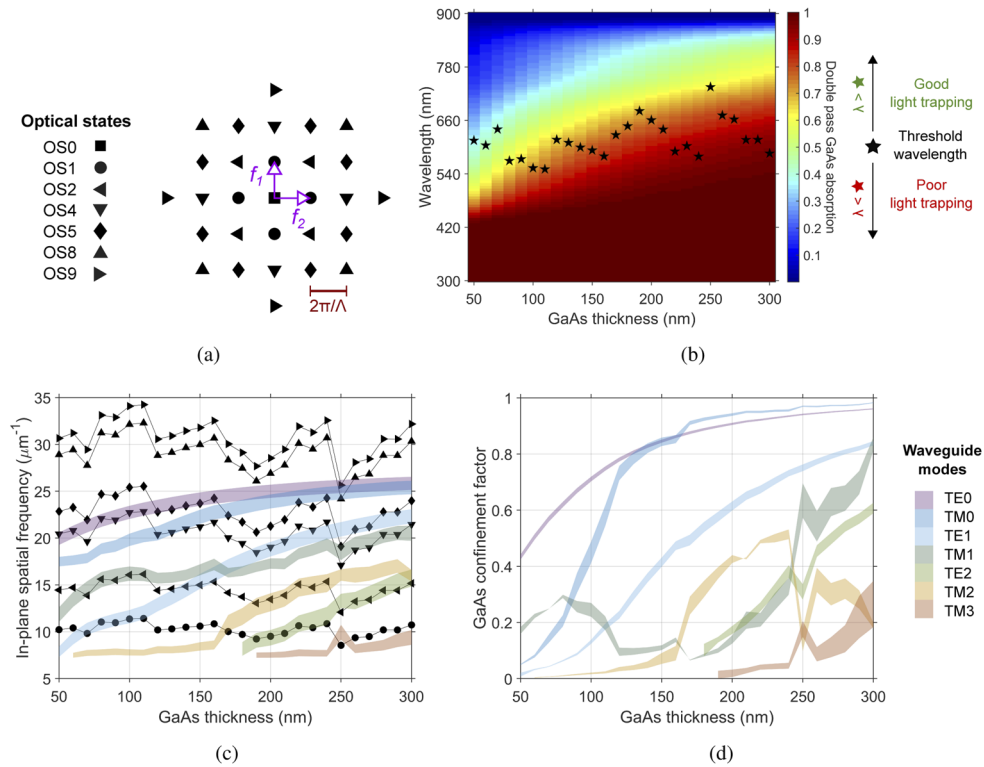


Fig. 5. (a) Reciprocal space representation of the square unit cells simulated in this work. (b) Threshold wavelength as a function of absorber thickness for the optimal devices shown in Fig. 4 with an Al_2O_3 (matrix) / $\text{In}_{0.47}\text{Al}_{0.53}\text{P}$ (feature) grating. Also shown is the double pass absorption in the GaAs active layer as a function of wavelength and absorber thickness. (c) Waveguide mode propagation constant as a function of absorber thickness for the optimal devices with an Al_2O_3 (matrix) / $\text{In}_{0.47}\text{Al}_{0.53}\text{P}$ (feature) grating shown in Fig. 4. The bands contain the spatial frequency regions where the propagation constants of the modes are found for $\lambda = 830 - 870$ nm. Also included are the spatial frequencies of OS1, OS2, OS4, OS5, OS8 and OS9 (marked as in (a)) for each optimal device at each absorber thickness, defined by their optimal pitch and Eq. (5). (d) Confinement factor (fraction of propagating power in the active layer) of the waveguide modes in (c), calculated just when the wave starts to propagate in the device stack.

the pitch) are those poorly absorbed in a double pass, and all shorter wavelengths have high double pass absorption so that losing power to air is not detrimental to device performance. Although useful for qualitatively explaining optimization results, the concept of a 'target' wavelength remains poorly defined since it is not clear what this wavelength should be for a given device architecture, or at what double pass absorption value light becomes sufficiently poorly absorbed to require good light trapping.

To further study the balance between double pass absorption and light trapping, threshold wavelengths are obtained from the device optimization results shown in Section 4 for the case of an Al_2O_3 (matrix) / $\text{In}_{0.47}\text{Al}_{0.53}\text{P}$ (feature) grating. The threshold wavelengths are identical to the optimal pitch (for a grating with a square unit cell) and are plotted in Fig. 5(b) as a function of absorber thickness. When overlaid onto a map of double pass absorption, it is clear that there is significant variation in the double pass absorption at the threshold wavelengths for different absorber thicknesses. In some optimal devices good light trapping is observed at all wavelengths

with double pass absorption $< 40\%$, whereas for some device thicknesses double pass absorption approaches 90% at the threshold wavelength. However, it seems that double pass absorption sets limits for the optimal pitch, as threshold wavelengths never occur where double pass absorption is $< 40\%$, and occur above 50% in most cases. Threshold wavelengths are also not seen where double pass absorption = 1. These results suggest that the concept of a ‘target’ wavelength cannot fully account for the trends in the optimal pitch of light trapping layers, in which case one could expect the threshold wavelength in Fig. 5(b) to simply track a certain double pass absorption value, increasing monotonically with absorber thickness. Instead, it is observed that the optimal pitch and associated threshold wavelength change in a stepwise manner, representing significant changes in optimal pitch with relatively small changes in absorber thickness (e.g. a 150 nm change in threshold wavelength for thicknesses between 250 and 300 nm). These steps occur within an overarching trend of increasing optimal pitch as device thickness increases.

To understand the variations in the optimal pitch, we turn to the other key light trapping mechanism: coupling incident illumination to waveguide modes. It has been shown previously that this mechanism can offer significant absorption enhancement and plays an important role in defining optimal light trapping layers for ultra-thin devices [35]. In particular, coupling to waveguide modes is essential near the absorber bandgap where the absorption coefficient is low. A waveguide mode exists in the device stack when constructive interference of light diffracted outside the escape cone allows the field to propagate through the stack. This interference condition is only met at certain in-plane wavevectors (or spatial frequencies) of light, normally called the propagation constants of the modes. For a given wavelength, each propagation constant will correspond to a different waveguide mode, with a characteristic distribution of the electric field in the device stack. Coupling incident illumination to a waveguide mode then occurs whenever light is diffracted at an optical state whose corresponding in-plane wavevector (given by Eq. (5)) matches the propagation constant of the mode. As a consequence, via Eq. (5) the pitch also plays an essential role in this light trapping mechanism.

To study whether this light trapping mechanism can explain the trends observed in the optimal pitch, we focus once again on the case of a device with an Al_2O_3 (matrix) / $\text{In}_{0.47}\text{Al}_{0.53}\text{P}$ (feature) grating. We calculate the waveguide modes of the optimal devices found in Section 4 for this material selection and for all the GaAs thicknesses studied. We do this for wavelengths in the range $\lambda = 830 - 870$ nm, close to the GaAs bandgap, and using the optimal fill factor and grating thickness. The bands in Fig. 5(c) show the spatial frequency range where the propagation constants of the calculated waveguide modes are found for the wavelength range of interest. Also included in the figure are markers which show the in-plane wavevectors (K_{xy}) corresponding to OS1, OS2, OS4, OS5, OS8 and OS9 according to Eq. (5) and the optimal pitch of each device at each absorber thickness (the OS shown are those with the lowest nonzero in-plane wavevectors). Whenever a marker lies within a band, coupling of incident illumination to the corresponding waveguide mode near the bandgap is possible.

Inspection of Fig. 5(c) reveals that the observed changes in the pitch are allowing the optical states to track the waveguide modes, ensuring that coupling events of near bandgap wavelengths to such optical modes are present and retained throughout the absorber thickness range studied. This tracking phenomenon occurs in a stepwise manner, driven by jumps in the optimal pitch. To aid in the interpretation of these results, we also calculated the confinement factor of the waveguide modes (Fig. 5(d)), defined as the fraction of the propagating power in the mode that is confined in the absorber layer. A high confinement is advantageous since more propagating power is constrained in the active layer where absorption enhancement is sought by light trapping mechanisms.

The results in Fig. 5(c) show that the optimal devices with absorber thicknesses < 120 nm have coupling events to TE0, TE1 and TM1, which are tracked mainly by OS4, OS1 and OS2, respectively. An exception is observed at an absorber thickness of 70 nm where it is OS5 which

is coupled to TE0. At such reduced length-scales, coupling to TE0 is essential as this mode has the highest confinement factor. At an absorber thickness of 120 nm a jump in the pitch shifts the coupling events. Coupling to TE0 and TE1 is retained, but now at OS5 and OS2, respectively. Coupling to TM1 is lost, as at this absorber thickness its confinement factor drops. Instead, a new coupling condition is introduced to TM0 at OS4, which is advantageous since at this point the confinement factor of this mode becomes high and comparable to that of TE0. The next shift in coupling conditions is observed beyond an absorber thickness of 160 nm, driven by another jump in the pitch. In this case coupling is observed mainly to TE1 (OS4), TM2 (OS2) and TE2 (OS1). Some coupling events to TM0 are also present. In this length-scale region the confinement factor of TE1 becomes significant (> 0.5) and that of TM2 also increases to reach > 0.3 . Finally, at an absorber thickness of 250 nm there is a considerable drop in the confinement factor of TM2 and a significant increase in that of TM1. Consequently, the final jump in the pitch at this absorber thickness then removes the previous coupling to TM2 but introduces coupling to TM1 at OS4. Other coupling events present in this length-scale are TE2 at OS2 and TE1 at OS5, both modes with high confinement in the absorber layer.

These results suggest that the stepwise variations in the optimal pitch of ultra-thin solar cells are driven by the modal structure of the device, seeking to enable maximum absorption enhancement for near bandgap wavelengths by retaining favourable coupling events to waveguide modes with high confinement factor in this spectral range. Jumps in the pitch shift the resonances in the device, whereas generally within the steps a gradual reduction in the pitch allows the K_{xy} of the sets of optical states to track the increasing propagation constant of the waveguide modes so that these resonances can be preserved as the absorber gets thicker. These variations in the optimal pitch occur within limits set by the double pass absorption in the absorber material, retaining good light trapping for wavelengths with $\lesssim 50\%$ absorption in a double pass. Introducing a short pitch to ensure that all wavelengths of interest experience good light trapping would not be beneficial, as this reduces the density of optical states in the devices and increases the number of evanescent optical states (with K_{xy} larger than the wavevector in the absorber, having no positive contributions to absorption enhancement).

To conclude, it is important to mention that the relative spatial frequencies of the optical states are fixed by Eq. (5), and so having favourable and multiple coupling events to waveguide modes to retain optimal performance is not trivial. Having the K_{xy} of an OS match the propagation constant of a mode fixes all other K_{xy} for all other OS. A good overlap between the distribution of optical states and the modal structure of a device will require corresponding changes in the pitch to alter the former (within the limits already discussed), and changes in the thickness of the ARC and the grating, as well as the fill factor, to alter the latter, as the propagation constants depend on the thickness and optical constants of all layers in the stack. However, these last parameters also need to be optimal for other phenomena such as reflection, parasitic absorption and scattering efficiency. Finally, it is important to mention that the threshold wavelength and optimal pitch trends discussed in this section were also observed after analysing the optimization results of Section 4 for other material combinations (see [Supplement 1](#)).

6. Conclusion

Ultra-thin photovoltaics offer many potential advantages, such as reduced materials usage for lower costs, flexible form factors, low mass for systems integration and intrinsic radiation tolerance for space power applications. However, careful light management is essential to boost solar absorption. Periodic nanostructures can be employed to diffract light outside the cone of escape at the front surface and localize the field within an ultra-thin absorber by coupling to waveguide modes. Metallic nanostructures have been widely studied for this application due to their scattering efficiency; however, parasitic absorption in the metal can limit efficiency gains. In this work we evaluated nonmetallic gratings for light trapping in ultra-thin solar cells, with a

view to minimizing parasitic losses in the scattering structures. This is achieved by simulating photocurrent from ultra-thin solar cells with integrated rear surface gratings made of materials with relatively low values of extinction coefficient in the wavelength region close to the absorption threshold of the solar cell material (i.e. high-bandgap semiconductors and dielectrics). GaAs solar cells between 50 nm and 300 nm active layer thickness were used as a model system for this study.

For each material combination, grating thickness, pitch and feature dimensions were optimized to obtain maximum current. It was found that the simulated optimized photocurrent could be predicted with an empirical model where the only inputs are the refractive index and extinction coefficient of the grating feature and the surrounding matrix material. While the benefits of having an efficient scattering structure were most pronounced for the thinnest devices, the functional form of the empirical model was preserved for all device thicknesses studied. The best material combinations had a large difference in average refractive index between feature and matrix material, and a small sum of the extinction coefficients, across the wavelength range of interest. These properties corresponded to pairings of dielectrics with high bandgap semiconductors, which made the gratings good scatterers and poor absorbers. Substituting the high bandgap semiconductor with other dielectrics reduced scattering efficiency and substituting with a lower bandgap semiconductor or a metal increased parasitic absorption, resulting in lower photocurrents.

Significantly, from a design perspective, these results show that grating materials can be selected independent of grating dimension considerations or absorber thickness. This design parameter independence allows the suitability of a material system to be immediately evaluated relative to other available alternatives, without the need for simulation and optimization of a large design space. The optimized photocurrent was also found to be relatively constant under exchange of the two grating materials, i.e. swapping the matrix and feature materials. As such, the order of material deposition or the use of etch process versus lift-off process can be guided purely by fabrication practicalities, as opposed to being fixed by the design requirements.

The best material combinations with efficient scattering but low absorption can be determined without fixing the grating or device dimensions; however, to achieve the highest photocurrent, the grating dimensions (pitch, fill factor, and thickness) must still be optimized for a given device thickness in order to (i) prevent diffraction into the cone of escape and (ii) promote coupling to waveguide modes, which localize the incident field in the absorber volume for longer wavelengths which are poorly absorbed on a double pass. Grating pitch selection is a balance of these two factors. In the case of a square grating, the lowest diffracted order will lie within the cone of escape for wavelengths shorter than the pitch. As such, an overarching trend is observed with optimal pitch increasing with increasing device thickness, as the double pass absorption of longer wavelengths increases and so the spectral range requiring absorption enhancement is pushed towards the bandgap of the absorber material. However, within the overarching trend, there is stepwise variation in optimal pitch. It is observed that the steps shift the coupling events to waveguide modes near the absorber bandgap in accordance with changes in their confinement factor. Within the steps the optimal pitch gradually changes to retain these resonances where diffracted orders are coupled to waveguide modes with high confinement in the absorber.

Given the complex relationship between optimal grating dimensions and device thickness, the independence of material selection drastically reduces the overall design space for these systems, making global optimization a tangible prospect.

Funding. H2020 European Research Council (853365); Consejo Nacional de Ciencia y Tecnología; Cambridge Trust; Engineering and Physical Sciences Research Council (EP/L015978/1).

Disclosures. The authors declare no conflicts of interest.

Data availability. Data underlying the results presented in this paper are not publicly available at this time but may be obtained from the authors upon reasonable request.

Supplemental document. See [Supplement 1](#) for supporting content.

References

1. L. Hirst, M. Yakes, J. Warner, M. Bennett, K. Schmieder, R. Walters, and P. Jenkins, "Intrinsic radiation tolerance of ultra-thin gaas solar cells," *Appl. Phys. Lett.* **109**(3), 033908 (2016).
2. K. R. Catchpole, S. Mookkapati, F. Beck, E. C. Wang, A. McKinley, A. Basch, and J. Lee, "Plasmonics and nanophotonics for photovoltaics," *MRS Bull.* **36**(6), 461–467 (2011).
3. I. Massiot, A. Cattoni, and S. Collin, "Progress and prospects for ultrathin solar cells," *Nat. Energy* **5**(12), 959–972 (2020).
4. V. K. Narasimhan and Y. Cui, "Nanostructures for photon management in solar cells," *Nanophotonics* **2**(3), 187–210 (2013).
5. M. A. Green and S. Pillai, "Harnessing plasmonics for solar cells," *Nat. Photonics* **6**(3), 130–132 (2012).
6. I. Massiot, N. Vandamme, N. Bardou, C. Dupuis, A. Lemaître, J.-F. Guillemoles, and S. Collin, "Metal nanogrid for broadband multiresonant light-harvesting in ultrathin gaas layers," *ACS Photonics* **1**(9), 878–884 (2014).
7. H.-L. Chen, A. Cattoni, R. De Lépinau, A. W. Walker, O. Höhn, D. Lackner, G. Siefert, M. Faustini, N. Vandamme, J. Goffard, B. Behaghel, C. Dupuis, N. Bardou, F. Dimroth, and S. Collin, "A 19.9%-efficient ultrathin solar cell based on a 205-nm-thick GaAs absorber and a silver nanostructured back mirror," *Nat. Energy* **4**(9), 761–767 (2019).
8. L. Sayre, E. Camarillo Abad, P. Pearce, P. Chausse, P.-M. Coulon, P. Shields, A. Johnson, and L. C. Hirst, "Ultrathin gaas solar cells with nanophotonic metal-dielectric diffraction gratings fabricated with displacement talbot lithography," *Prog. Photovoltaics: Res. Appl.* (2021).
9. P. Pearce, A. Mellor, and N. Ekins-Daukes, "The importance of accurate determination of optical constants for the design of nanometallic light-trapping structures," *Sol. Energy Mater. Sol. Cells* **191**, 133–140 (2019).
10. M. L. Brongersma, Y. Cui, and S. Fan, "Light management for photovoltaics using high-index nanostructures," *Nat. Mater.* **13**(5), 451–460 (2014).
11. J. Buencuerpo, M. A. Steiner, and A. C. Tamboli, "Optically-thick 300 nm gaas solar cells using adjacent photonic crystals," *Opt. Express* **28**(9), 13845–13860 (2020).
12. J. Buencuerpo, J. M. Llorens, J. M. Ripalda, M. A. Steiner, and A. C. Tamboli, "Engineering the reciprocal space for ultrathin gaas solar cells," *Opt. Laser Technol.* **142**, 107224 (2021).
13. J. R. D’Rozario, S. J. Polly, G. T. Nelson, and S. M. Hubbard, "Thin gallium arsenide solar cells with maskless back surface reflectors," *IEEE J. Photovoltaics* **10**(6), 1681–1688 (2020).
14. M. van Eerden, G. J. Bauhuis, P. Mulder, N. Gruginskie, M. Passoni, L. C. Andreani, E. Vlieg, and J. J. Schermer, "A facile light-trapping approach for ultrathin gaas solar cells using wet chemical etching," *Prog. Photovoltaics: Res. Appl.* **28**(3), 200–209 (2020).
15. P. Bermel, C. Luo, L. Zeng, L. C. Kimerling, and J. D. Joannopoulos, "Improving thin-film crystalline silicon solar cell efficiencies with photonic crystals," *Opt. Express* **15**(25), 16986 (2007).
16. J. Grandidier, D. M. Callahan, J. N. Munday, and H. A. Atwater, "Light absorption enhancement in thin-film solar cells using whispering gallery modes in dielectric nanospheres," *Adv. Mater.* **23**(10), 1272–1276 (2011).
17. P. Spinelli, M. Verschuuren, and A. Polman, "Broadband omnidirectional antireflection coating based on subwavelength surface mie resonators," *Nat. Commun.* **3**(1), 692–695 (2012).
18. S.-M. Lee, A. Kwong, D. Jung, J. Faucher, R. Biswas, L. Shen, D. Kang, M. L. Lee, and J. Yoon, "High performance ultrathin gaas solar cells enabled with heterogeneously integrated dielectric periodic nanostructures," *ACS Nano* **9**(10), 10356–10365 (2015).
19. Y. Peng and S. Gong, "Light-trapping structure based on ultra-thin gaas solar cell," *J. Phys. D: Appl. Phys.* **53**(49), 495107 (2020).
20. A. P. Vasudev, J. A. Schuller, and M. L. Brongersma, "Nanophotonic light trapping with patterned transparent conductive oxides," *Opt. Express* **20**(S3), A385–A394 (2012).
21. A. Mavrokefalos, S. E. Han, S. Yerci, M. S. Branham, and G. Chen, "Efficient light trapping in inverted nanopillar thin crystalline silicon membranes for solar cell applications," *Nano Lett.* **12**(6), 2792–2796 (2012).
22. K. X. Wang, Z. Yu, V. Liu, Y. Cui, and S. Fan, "Absorption enhancement in ultrathin crystalline silicon solar cells with antireflection and light-trapping nanocone gratings," *Nano Lett.* **12**(3), 1616–1619 (2012).
23. S. E. Han and G. Chen, "Optical absorption enhancement in silicon nanohole arrays for solar photovoltaics," *Nano Lett.* **10**(3), 1012–1015 (2010).
24. S. E. Han and G. Chen, "Toward the lambertian limit of light trapping in thin nanostructured silicon solar cells," *Nano Lett.* **10**(11), 4692–4696 (2010).
25. M. Kroll, S. Fahr, C. Helgert, C. Rockstuhl, F. Lederer, and T. Pertsch, "Employing dielectric diffractive structures in solar cells—a numerical study," *phys. stat. sol. (a)* **205**(12), 2777–2795 (2008).
26. K. W. Robertson, R. R. LaPierre, and J. J. Krich, "Efficient wave optics modeling of nanowire solar cells using rigorous coupled-wave analysis," *Opt. Express* **27**(4), A133 (2019).
27. O. Isabella, R. Vismara, D. N. Linssen, K. X. Wang, S. Fan, and M. Zeman, "Advanced light trapping scheme in decoupled front and rear textured thin-film silicon solar cells," *Sol. Energy* **162**, 344–356 (2018).
28. H. Chung, C. Zhou, X. T. Tee, K.-Y. Jung, and P. Bermel, "Hybrid dielectric light trapping designs for thin-film CdZnTe/Si tandem cells," *Opt. Express* **24**(14), A1008 (2016).
29. Ioffe Institute, NSM Semiconductor Archive, (2021).

30. G. Yu, G. Wang, H. Ishikawa, M. Umeno, T. Soga, T. Egawa, J. Watanabe, and T. Jimbo, "Optical properties of wurtzite structure GaN on sapphire around fundamental absorption edge (0.78–4.77 eV) by spectroscopic ellipsometry and the optical transmission method," *Appl. Phys. Lett.* **70**(24), 3209–3211 (1997).
31. B. Johs, C. Herzinger, J. Dinan, A. Cornfeld, and J. Benson, "Development of a parametric optical constant model for $\text{Hg}_{1-x}\text{Cd}_x\text{Te}$ for control of composition by spectroscopic ellipsometry during MBE growth," *Thin Solid Films* **313-314**, 137–142 (1998).
32. Y. Jiang, S. Pillai, and M. A. Green, "Realistic Silver Optical Constants for Plasmonics," *Sci. Rep.* **6**(1), 30605 (2016).
33. P. M. Pearce, "Rayflare: flexible optical modelling of solar cells," *J. Open Source Softw.* **6**(65), 3460 (2021).
34. V. Liu and S. Fan, "S4 : A free electromagnetic solver for layered periodic structures," *Comput. Phys. Commun.* **183**(10), 2233–2244 (2012).
35. E. Camarillo Abad, H. J. Joyce, and L. C. Hirst, "Light management in ultra-thin solar cells: a guided optimisation approach," *Opt. Express* **28**(26), 39093–39111 (2020).